IEEE Robotics and Automation Letters (RA-L) paper, presented at ICRA 2024, Yokohama, Japan. Cite as RA-L paper.

Proprioceptive-based Whole-body Disturbance Rejection Control for Dynamic Motions in Legged Robots

Zhengguo Zhu[1], Guoteng Zhang[1], Zhongkai Sun[1], Teng Chen[1], Xuewen Rong[1], Anhuan Xie[2], Yibin Li[1]

***Abstract*—This paper presents a control framework for legged robots that enables self-perception and resistance to external disturbances. First, a novel proprioceptive-based disturbance estimator is proposed. Compared with other disturbance estimators, this estimator possesses notable advantages in terms of filtering foot-ground interaction noise and suppressing the accumulation of estimation errors. Additionally, our estimator is a fully proprioceptive-based estimator, eliminating the need for any exteroceptive devices or observers. Second, we present a hierarchical optimized whole-body controller (WBC), which takes into account the full body dynamics, the actuation limits, the external disturbances, and the interactive constraints. Finally, extensive experimental trials conducted on the point-foot biped robot BRAVER validate the capabilities of the proposed estimator and controller under various disturbance conditions.**

***Index Terms*—Legged robots, disturbances estimation, whole-body control.**

I. Introduction

LEGGED robots have always gained widespread interest in the robotics community because they can navigate challenging terrain where wheeled or tracked robots cannot. This enables them to be deployed in a wider range of applications. When robots perform tasks in the working environment, they inevitably experience external disturbances such as pushing, collisions, and even changes in load. These external disturbances can cause the robot to deviate from the predefined trajectory, and even fall over. Thus, possessing the capability to resist external disturbances is a valuable skill for maintaining stable locomotion. To enhance robot robustness, a variety of methods for rejecting disturbances have been developed and implemented [1]–[6]. Numerous methods utilize joint-specific torque compensation to mitigate external disturbances. For example, Yi et al. [1] proposes a control strategy that involves adjusting the ankle, hip, and step to counteract external disturbances. Prahlad et al. [2] used force sensors to calculate a compensating torque injected into ankle-joint to diminish the influence of disturbances. In addition, utilizing foot force planning for disturbance rejection is a common method as well. Hyon et al. [3] proposed a passivity-based contact force control method with gravity compensation. Wang et al. [4] proposed a CoM compliant controller for stable standing of humanoid robots in the presence of unknown disturbances. Another frequently employed approach for disturbance rejection involves mitigating disturbances by dynamically adjusting the support configuration through step-taking. Pratt et al. [5] implemented a method that calculates the Capture Point and Capture Region to prevent the robot from falling when subjected to external forces. Dafarra et al. [6] deployed a momentum-based torque controller based on the Capture Point concept on the iCub robot to counteract external disturbances. However, these algorithms lack accurate external disturbance estimation and rely on state feedback for control strategy adjustments. As a result, their effectiveness in resisting larger external disturbances is limited.

The general momentum (GM) observer [7] is a powerful method for disturbance perception. This approach is initially developed for collision detection and disturbance perception in manipulator arm systems [8]. In recent years, it has been widely deployed on legged systems [9]–[12]. For example, Englsberger et al. [9] developed a disturbance estimator based on the concept of GM, enables the TORO robot to resist 15 % of its body weight external disturbances in simulation [10]. Focchi et al. extended the algorithm proposed in [10] to the angular case by estimating the complete wrench at the Center of Mass (CoM) and implemented it on the quadruped robot HyQ [11]. Morlando et al. proposed a momentum-based observer that enabled the quadruped robot DogBot to accurately perceive disturbances in simulation [12]. These methods are primarily employed for estimating disturbances in stationary or quasi-static gait motions, with limited application in dynamic gait scenarios. Nevertheless, dynamic gait is imperative for legged robots when faced with specific demands, such as expeditious transportation of objects. In dynamic gait scenarios, the rapid interaction between the foot and the ground introduces significant noise to the disturbances estimation of the base. When using momentum-based observers, these noises can only be filtered out if the filter's cutoff frequency is set close to the gait frequency, but this leads to noticeable reduction in signal amplitude. Additionally, the aforementioned GM based

Manuscript received: June 1, 2023; Revised August, 2, 2023; Accepted September, 13, 2023.

This paper was recommended for publication by Editor Jaydev P. Desai upon evaluation of the Associate Editor and Reviewers' comments. This work was supported by the National Key Research and Development Program of China (2022YFB4701504), the National Natural Science Foundation of China (91948201, 62003190) and the Open Research Projects of Zhejiang Lab (NO. 2022NB0AB06) (Corresponding author: Guoteng Zhang).

[1] Zhengguo Zhu, Guoteng Zhang, Zhongkai Sun, Teng Chen, Xuewen Rong and Yibin Li are with the School of Control Science and Engineering, Shandong University, Jinan 250061, China, (email: zgzhu1995@gmail.com; guoteng@email.sdu.edu.cn; lysunzhongkai@163.com; chenteng100@sdu.edu.cn; rongxw@sdu.edu.cn; liyb@sdu.edu.cn)

[2] Anhuan Xie is with the Intelligent Robot Research Centre, Zhejiang Lab, Hangzhou 311121, China, (email: xieanhuan@zhejianglab.com)

Digital Object Identifier (DOI): see top of this page.

IEEE Robotics and Automation Letters (RA-L) paper, presented at ICRA 2024, Yokohama, Japan. Cite as RA-L paper.

IEEE Robotics and Automation Letters (RA-L) paper, presented at ICRA 2024, Yokohama, Japan. Cite as RA-L paper.

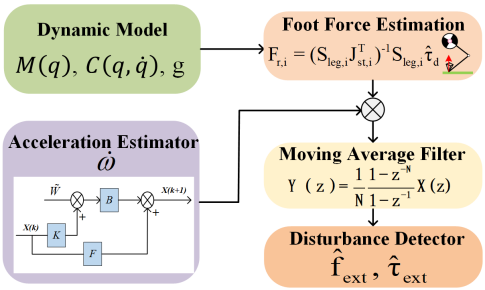

Fig. 1. Overview of the disturbance calculation.

methods all require the robot to be equipped with additional force sensors attached to robot's feet, which greatly reduces the algorithm's versatility across multiple platforms.

To address this issue, we develop a novel disturbance estimator. Our scheme is a departure from previous works in that the proposed estimator is fully proprioception-based and considers the impact of leg motions on estimating disturbances acting on the base. Learned from [13], the robot's performance is significantly affected by the control bandwidth, particularly in highly dynamic locomotion scenarios. To achieve robust motion under disturbance conditions, we propose a whole-body disturbance rejection controller with advantages in efficient computing. The main contributions and important emphases are the following:

1) A novel disturbance estimator has been introduced, capable of mitigating the impact of leg motion on disturbance estimation and suppressing error accumulation.
2) A hierarchically optimized whole-body disturbance rejection control framework is proposed, which comprehensively considers both full-body dynamics and system constraints.
3) Extensive experimental are conducted on the point-foot biped robot BRAVER [14] to demonstrate the capabilities of the proposed estimator and controller under various disturbance conditions.

This paper is organized as follows. Section II presents the mathematical derivation of the disturbance estimator. Section III introduces the whole-body disturbance rejection controller. Section IV and Section V evaluate the proposed framework's performance in simulation and physical prototype, respectively. Finally, Section VI provides the conclusion of this article.

II. Disturbances Estimator

The current mainstream legged robot disturbance estimators do not take into account the influence of periodic leg movements on body disturbance estimation, limiting their estimation accuracy in dynamic gait scenarios. Additionally, the GM-based disturbance observer has limitations in noise suppression and error accumulation due to the presence of an integrator. In this section, a novel disturbance estimator capable of alleviating the aforementioned issues is proposed. The overview of our developed disturbance estimator is depicted in Fig. 1.

A. Robot Dynamics

When the robot moves in the environment, its resultant dynamic model can be written as

$$\boldsymbol{M}\ddot{\boldsymbol{q}} + \boldsymbol{C}\dot{\boldsymbol{q}} + \boldsymbol{g} = \mathbf{S}^T\boldsymbol{\tau} + \boldsymbol{J}_{\text{st}}^T\boldsymbol{F}_{\text{r}} \tag{1}$$

where $\boldsymbol{M} \in \mathbb{R}^{(6+n)\times(6+n)}$, $\boldsymbol{C} \in \mathbb{R}^{(6+n)\times(6+n)}$, $\boldsymbol{g} \in \mathbb{R}^{6+n}$ are the inertia matrix, Coriolis matrix and gravity vector, respectively; $\boldsymbol{S} = \begin{bmatrix} \boldsymbol{O}_{n\times 6} & \boldsymbol{I}_n \end{bmatrix}$ is the actuated part selection matrix; $\boldsymbol{\tau} \in \mathbb{R}^{(n)}$ is the acutation torques; $\boldsymbol{F}_r \in \mathbb{R}^{3n_c}$ is the ground reaction forces (GRFs) of i-th leg; $\boldsymbol{J}_{st} \in \mathbb{R}^{3n_c\times(6+n)}$ is the Jacobians that transposes the GRFs into the acceleration of the COM and the actuated joints; n and n_c represents the number of active degrees of freedom (DoF) and the number of legs in the support state, respectively. In our work, $\boldsymbol{C}$ is considered as a non-linear term associated with $\boldsymbol{q}$ and $\dot{\boldsymbol{q}}$.

B. Interaction Force Estimation

The proprioceptive-based interaction force estimation method was firstly proposed in [15] and Bledt et al. extended it to contact estimation for legged robots [16]. In our work, we use a discrete-time version proposed in [16] to perceive real-time plantar forces.

Extracting the joint motion part of (1) we can get:

$$\boldsymbol{S}_\theta\left(\boldsymbol{M}\ddot{\boldsymbol{q}} + \boldsymbol{C}\dot{\boldsymbol{q}} + \boldsymbol{g}\right) = \boldsymbol{\tau} + \boldsymbol{S}_\theta\boldsymbol{J}_{st}^T\boldsymbol{F}_r \tag{2}$$

here, $\boldsymbol{S_\theta} \in \mathbb{R}^{n\times(n+6)}$ is the selection matrix for the limbs' components. Consider the force transmitted by all contact point as an external disturbance, and define a vector to represent it

$$\boldsymbol{\tau}_{\text{d}} = \boldsymbol{S}_\theta\boldsymbol{J}_{\text{st}}^T\boldsymbol{F}_{\text{r}} \tag{3}$$

In order to reduce the effect of high-frequency noise, a filtered version of this vector $\hat{\boldsymbol{\tau}}_d$ can be computed as

$$\hat{\boldsymbol{\tau}}_d = \frac{(1-\gamma)}{1-\gamma z^{-1}}\boldsymbol{\tau}, \gamma = \mathrm{e}^{-\lambda\Delta t} \tag{4}$$

where z is the z-domain variable, and Δt represents the sampling period; and λ represents the cutoff frequency of the filter. As described in [15], $\frac{(1-\gamma)}{1-\gamma z^{-1}}\boldsymbol{M}\ddot{\boldsymbol{q}}$ can be solved by

$$\frac{(1-\gamma)}{1-\gamma z^{-1}}\boldsymbol{M}\ddot{\boldsymbol{q}} = \beta\boldsymbol{\rho} - \frac{(1-\gamma)}{1-\gamma z^{-1}}\left(\boldsymbol{C}^T\dot{\boldsymbol{q}} + \boldsymbol{C}\dot{\boldsymbol{q}} + \beta\boldsymbol{\rho}\right) \tag{5}$$

where $\boldsymbol{\rho} = \boldsymbol{M}\dot{\boldsymbol{q}}$ is the generalized momentum and $\beta = (1-\gamma)\gamma^{-1}/\Delta t$. Moreover, it is assumed that $\boldsymbol{\rho}(0) = \mathbf{0}$, which means that the observer's kick off should be prior to the robot control. Thus, (4) can be rewriten as

$$\hat{\boldsymbol{\tau}}_{\text{d}} = \beta\boldsymbol{S}_\theta\boldsymbol{\rho} - \frac{(1-\gamma)}{1-\gamma z^{-1}}\boldsymbol{S}_\theta\left(\beta\boldsymbol{\rho} + \boldsymbol{S}^T\boldsymbol{\tau} + \boldsymbol{C}^T\dot{\boldsymbol{q}} - \boldsymbol{g}\right) \tag{6}$$

Then, the interaction force of each leg can be calculated through

$$\boldsymbol{F}_{\text{r,i}} = \left(\boldsymbol{S}_{\text{leg,i}}\boldsymbol{J}_{\text{st,i}}^T\right)^{-1}\boldsymbol{S}_{\text{leg,i}}\hat{\boldsymbol{\tau}}_{\text{d}} \tag{7}$$

where $\boldsymbol{S}_{\text{leg,i}}$ is the selector matrix for the joints in limb i and $\boldsymbol{J}_{\text{st,i}}$ is the Jacobian matrix for i-th supporting leg ; and $\boldsymbol{F}_{\text{r,i}}$ is the GRFs of i-th supporting leg;

IEEE Robotics and Automation Letters (RA-L) paper, presented at ICRA 2024, Yokohama, Japan. Cite as RA-L paper.

IEEE Robotics and Automation Letters (RA-L) paper, presented at ICRA 2024, Yokohama, Japan. Cite as RA-L paper.

C. COM External Wrench Estimation

As dicussed in [17], compared with body velocity, body acceleration is a preferred indicator for reflecting impact-type disturbances. Furthermore, compared to momentum-based observers, utilizing acceleration directly for disturbance estimation avoids integrators, reducing errors accumulation. Thus, in this project, we choose to use acceleration for disturbance estimation and proposed a novel approach to address the issue of unavailability of Euler angular acceleration in the inertial measurement unit (IMU). That is organizing acceleration into the state vector of the Kalman equations, thereby achieving dynamic estimation of angular acceleration.

According to the Newton-Euler equations, the dynamics of the robot's CoM can be expanded as

$$\ddot{\boldsymbol{c}} = \frac{1}{M}\left(\sum_{i=1}^{n_c} \boldsymbol{F}_{\mathrm{r,i}} + \boldsymbol{f}_{\mathrm{ext}}\right) + \boldsymbol{a}_{\mathcal{G}} \tag{8}$$

$$\frac{\boldsymbol{d}}{\boldsymbol{dt}}(\boldsymbol{I\omega}) = \sum_{i=1}^{n_c} (\boldsymbol{p}_{\mathrm{i}} - \boldsymbol{c}) \times \boldsymbol{F}_{\mathrm{r,i}} + \boldsymbol{\tau}_{\mathrm{ext}} \tag{9}$$

where $\boldsymbol{a}_{\mathcal{G}}$ represents the acceleration due to gravity; $\boldsymbol{c}$ is the position of the robot's CoM in the world frame; $\boldsymbol{I}$ is the centroidal rotational inertia; $\boldsymbol{\omega}$ is the angular velocity of the base in the world frame; $\boldsymbol{p}_i$ is the position of the i-th supporting leg in the world frame; M is the total robot's mass; and $\boldsymbol{f}_{\mathrm{ext}}$ and $\boldsymbol{\tau}_{\mathrm{ext}}$ represent the external forces and torques exerted on the base, respectively. Since the linear acceleration of the body can be directly measured by the IMU, the external force acting on the body can be calculated by

$$\hat{\boldsymbol{f}}_{ext} = \frac{(1-\gamma)}{1-\gamma z^{-1}}\left(M\left(\ddot{\boldsymbol{c}} - \boldsymbol{a}_{\mathcal{G}}\right) - \sum_{i=1}^{n_c} \boldsymbol{F}_{\mathrm{r,i}}\right) \tag{10}$$

where $\hat{\boldsymbol{f}}_{\mathrm{ext}}$ is the estimated value of $\boldsymbol{f}_{\mathrm{ext}}$.

Expressing the system equations of the Kalman Filter (KF) in a discrete state-space form leads to the following result:

$$\begin{cases} \boldsymbol{X}_k = \boldsymbol{F}\boldsymbol{X}_{k-1} + \boldsymbol{B}\boldsymbol{U}_k + \boldsymbol{W}_{k-1} \\ \boldsymbol{Z}_k = \boldsymbol{H}\boldsymbol{X}_k + \boldsymbol{V}_{k-1} \end{cases} \tag{11}$$

where $\boldsymbol{F}$ and $\boldsymbol{B}$ are the state transition matrix and input matrix, respectively. $\boldsymbol{W}_{k-1}$ and $\boldsymbol{V}_{k-1}$ are system noise vector and measurement noise vector, respectively, which are usually assumed to be uncorrelated Gaussian noise

$$\begin{cases} \boldsymbol{W} \sim \mathcal{N}(0, \boldsymbol{Q}) \\ \boldsymbol{V} \sim \mathcal{N}(0, \boldsymbol{R}) \end{cases} \tag{12}$$

where $\boldsymbol{Q}$ and $\boldsymbol{R}$ are the system noise variance and measurement noise variance, respectively. we define $\boldsymbol{X} = \begin{bmatrix} \boldsymbol{\varphi}^T & \boldsymbol{\omega}^T & \dot{\boldsymbol{\omega}}^T \end{bmatrix}^T$ as the state variable of the system, where $\boldsymbol{\varphi}$ is the orientation angle aligned with the coordinate system of $\boldsymbol{\omega}$. A numerical solution method is employed here to approximate the linearization of angular dynamics.. The input vector $\boldsymbol{U}$ is defined as $\boldsymbol{U} = \begin{bmatrix} \ddot{\boldsymbol{\varphi}} \end{bmatrix}$ and the output vector $\boldsymbol{Z}$ is defined as $\boldsymbol{Z} = \begin{bmatrix} \boldsymbol{\varphi}^T & \boldsymbol{\omega}^T \end{bmatrix}^T$. The state transition matrix $\boldsymbol{F}$ and input matrix $\boldsymbol{B}$ are given by:

$$\boldsymbol{F} = \begin{bmatrix} \boldsymbol{I}_3 & \Delta t * \boldsymbol{I}_3 & \frac{\Delta t^2}{2} * \boldsymbol{I}_3 \\ 0 & \boldsymbol{I}_3 & \Delta t * \boldsymbol{I}_3 \\ 0 & 0 & \boldsymbol{I}_3 \end{bmatrix}, \boldsymbol{B} = \begin{bmatrix} \frac{\Delta t^3}{6} * \boldsymbol{I}_3 \\ \frac{\Delta t^2}{2} * \boldsymbol{I}_3 \\ \Delta t * \boldsymbol{I}_3 \end{bmatrix} \tag{13}$$

where $\boldsymbol{I}_3$ denotes the 3×3 identity matrix. The observation matrix is given by:

$$\boldsymbol{H} = \begin{bmatrix} \boldsymbol{I}_3 & 0 & 0 \\ 0 & \boldsymbol{I}_3 & 0 \end{bmatrix} \tag{14}$$

Since multiple differentiation of the signal will seriously amplify the noise, the higher-order terms of $\boldsymbol{\varphi}$ cannot be accurately obtained in practice. In this paper, we introduce a novel simplification scheme by treating $\boldsymbol{BU}$ as Gaussian noise and combining it with $\boldsymbol{W}$ as a new Gaussian white noise term $\widetilde{\boldsymbol{W}}$. According to (9), the KF's input $\ddot{\boldsymbol{\varphi}}$ is a function of $\boldsymbol{F}_r$, $\dot{\boldsymbol{F}}_r$, and $\dot{\boldsymbol{\tau}}_{ext}$, which can be expressed as: $\ddot{\boldsymbol{\varphi}} = \mathcal{F}\left(\boldsymbol{F}_r, \dot{\boldsymbol{F}}_r, \dot{\boldsymbol{\tau}}_{ext}\right)$. Considering physical constraints and the robot's deployment environment, both $\dot{\boldsymbol{F}}_r$ and $\dot{\boldsymbol{\tau}}_{ext}$ are bounded. Additionally, legged robot controllers must maintain higher update frequencies, especially during high-dynamic locomotion scenarios. Therefore, during actual deployment, both $\Delta t^2 * \ddot{\boldsymbol{\varphi}}$ and its higher-order term $\Delta t^3 * \dddot{\boldsymbol{\varphi}}$ are negligible. Consequently, we approximate $\boldsymbol{BU}$ as follows:

$$\boldsymbol{BU} = \begin{bmatrix} \frac{\Delta t^3}{6} * \boldsymbol{I}_3 \\ \frac{\Delta t^2}{2} * \boldsymbol{I}_3 \\ \Delta t * \boldsymbol{I}_3 \end{bmatrix} \cdot \ddot{\boldsymbol{\varphi}} \approx \begin{bmatrix} 0 \\ 0 \\ \Delta t * \ddot{\boldsymbol{\varphi}} \end{bmatrix} \tag{15}$$

Thus, $\widetilde{\boldsymbol{W}}$ can be computed through:

$$\widetilde{\boldsymbol{W}} = \begin{bmatrix} \boldsymbol{W}_{\varphi} \\ \boldsymbol{W}_{\omega} \\ \Delta t * \ddot{\boldsymbol{\varphi}} + \boldsymbol{W}_{\dot{\omega}} \end{bmatrix} \tag{16}$$

where $\boldsymbol{W}_{\varphi}$, $\boldsymbol{W}_{\omega}$, and $\boldsymbol{W}_{\dot{\omega}}$ are process noise terms for $\boldsymbol{\varphi}$, $\boldsymbol{\omega}$, and $\dot{\boldsymbol{\omega}}$, respectively. These terms can all be estimated by analyzing the dynamic characteristics of the system. $\Delta t * \ddot{\boldsymbol{\varphi}}$ can be estimated based on the system's control frequency and its own maximum tolerable disturbance. By adding appropriate process noise $\widetilde{\boldsymbol{W}}$ and observation noise $\boldsymbol{V}$, the iteration process of KF can be utilized for estimating the angular acceleration $\dot{\boldsymbol{\omega}}$. Then, computing the external torque with:

$$\hat{\boldsymbol{\tau}}_{\mathrm{ext}} = \frac{(1-\gamma)}{1-\gamma z^{-1}}\left(\frac{\boldsymbol{d}}{\boldsymbol{dt}}(\boldsymbol{I\omega}) - \sum_{i=1}^{n_c} (\boldsymbol{p}_i - \boldsymbol{c}) \times \boldsymbol{F}_{\mathrm{r,i}}\right) \tag{17}$$

where $\hat{\boldsymbol{\tau}}_{\mathrm{ext}}$ is the estimated value of $\boldsymbol{\tau}_{\mathrm{ext}}$. Excluding eq (17) from KF is due to the potential importance of $\dot{\boldsymbol{\omega}}$ as feedback for specific algorithms.

D. Moving Average Filter

The robot's foot-ground interaction is a strong impact process, leading to unavoidable errors in estimating the interaction force. In addition, potential modeling errors can also result in inaccurate mapping of forces. These errors can be propagated to base and decrease the accuracy of disturbance estimation. Given the inherent periodicity of leg movements in legged robots, the disturbance estimation noise caused by the aforementioned errors also exhibits periodic oscillations. To mitigate the adverse effects of this noise, we incorporated a Moving Average Filter (MAF) into the disturbance estimator. The specific expression of the filter is as follows

$$Y(z) = \frac{1}{N}\frac{1-z^{-N}}{1-z^{-1}}X(z) \tag{18}$$

IEEE Robotics and Automation Letters (RA-L) paper, presented at ICRA 2024, Yokohama, Japan. Cite as RA-L paper.

IEEE Robotics and Automation Letters (RA-L) paper, presented at ICRA 2024, Yokohama, Japan. Cite as RA-L paper.

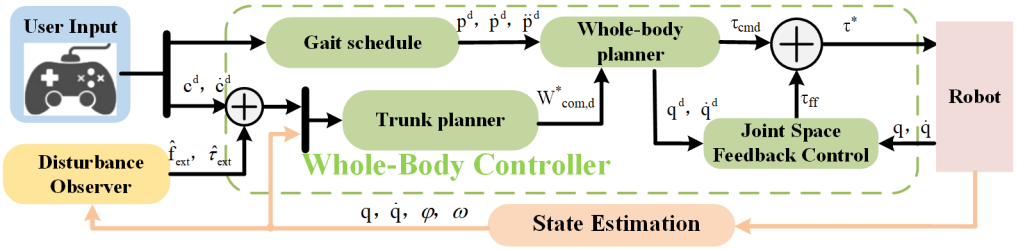

Fig. 2. Diagram of the disturbance rejection whole body control scheme. $\boldsymbol{c}^{\mathrm{d}}$ and $\dot{\boldsymbol{c}}^{\mathrm{d}}$ represent the desired position and desired velocity of the robot base, respectively; $\boldsymbol{p}^{\mathrm{d}}$, $\dot{\boldsymbol{p}}^{\mathrm{d}}$, and $\ddot{\boldsymbol{p}}^{\mathrm{d}}$ represent the desired position, desired velocity, and desired acceleration of the swing leg's foot, respectively.

where $z = e^{j\omega T_s}$; N is the sliding window width, $X(z)$ is the input value at the current sampling moment and $Y(z)$ is the filtered value at this moment. In this case, the value N is set to be positively correlated with the gait cycle T. That is, $N * \Delta t$ is an integer multiple of T. This configuration helps to counteract the interference caused by periodic leg motion on the disturbance estimation of the base. In practical implementation, the activation of the MAF can be adjusted according to specific needs. During high step frequency locomotion, the noise suppression advantages of MAF are evident, and this will be further proved in our experimental section.

III. Locomotion Controller

In this section we present and formulate our locomotion controller. Fig. 2 depicts the main components of our locomotion framework. When specifying the desired robot motion state, the trunk planner and gait scheduler generate reference trajectories online and provide them to the whole-body planner. These references consist of desired trajectories for the CoM, body orientation and the foot swing curves. The state estimation combines leg odometry and inertial sensing to provide the controller with an estimated representation of the robot's state. The disturbance observer provides the trunk planner with a reference value for disturbance compensation. The trunk planner provides a CoM desired wrench feedforward term to the whole-body planner and the whole-body planner performs hierarchical acceleration command planning. The WBC balance them by computing the optimal generalized accelerations and contact forces via Quadratic Program (QP) and mapping them to the desired joint torques while taking into account the full body level dynamics of the robot and the friction constraints.

A. Trunk planner

Due to the unpredictable and time-varying nature of external disturbances, we utilize the virtual model controller proposed in [11] for compensating disturbances, which provides advantages in enhancing system control bandwidth. Recalling the first 6 rows in (1) and defining the gravito-inertial CoM wrench as $\boldsymbol{W}_{\mathrm{com}} = \boldsymbol{S}_{\mathrm{f}}\left(\boldsymbol{M}\ddot{\boldsymbol{q}} + \boldsymbol{C}\dot{\boldsymbol{q}} + \boldsymbol{g}\right)$, we can express the floating-base dynamics as follows:

$$\boldsymbol{W}_{\mathrm{com}} = \boldsymbol{J}_{\mathrm{st,com}}^{T}\boldsymbol{F}_{\mathrm{r}} \tag{19}$$

where $\boldsymbol{S}_{\mathrm{f}}$ is the floating base selection matrix and $\boldsymbol{J}_{\mathrm{st,com}}$ maps $\boldsymbol{F}_{\mathrm{r}}$ to the CoM wrench space. To achieve a desired motion of the base, we perform online disturbance compensation in the trunk planner:

$$\boldsymbol{J}_{\mathrm{st,com}}^{T}\boldsymbol{F}_{\mathrm{r}} = \boldsymbol{W}_{\mathrm{com}}^{\mathrm{d}} \tag{20}$$

with

$$\boldsymbol{F}_{\mathrm{r}} = \begin{pmatrix} \boldsymbol{F}_{r,1} \\ \boldsymbol{F}_{r,2} \\ \vdots \\ \boldsymbol{F}_{r,n_c} \end{pmatrix}, \boldsymbol{W}_{\mathrm{com}}^{\mathrm{d}} = \boldsymbol{K}_{\mathrm{p}}\Delta\boldsymbol{c} + \boldsymbol{K}_{\mathrm{d}}\Delta\dot{\boldsymbol{c}} + \boldsymbol{W}_{\mathrm{g}} - \boldsymbol{W}_{\mathrm{ext}} \tag{21}$$

where $-\boldsymbol{W}_{\mathrm{ext}} = \begin{bmatrix} -\hat{\boldsymbol{f}}_{\mathrm{ext}}^{T} & -\hat{\boldsymbol{\tau}}_{\mathrm{ext}}^{T} \end{bmatrix}^{T}$ is a compensation term for external disturbances; $\boldsymbol{K}_{\mathrm{p}}$ and $\boldsymbol{K}_{\mathrm{d}}$ are positive-define diagonal matrices of proportional and derivative gains, respectively; $\boldsymbol{W}_{\mathrm{g}}$ is the gravity compensation wrench; $\Delta\boldsymbol{c} = \boldsymbol{c}_{\mathrm{com,d}} - \boldsymbol{c}_{\mathrm{com}}$ and $\Delta\dot{\boldsymbol{c}} = \dot{\boldsymbol{c}}_{\mathrm{com,d}} - \dot{\boldsymbol{c}}_{\mathrm{com}}$ are the tracking errors of the position and velocity of the base.

To distribute the load on the stance feet while respecting the specified constraints, we formulate the QP:

$$\begin{aligned} \boldsymbol{F}_{\mathrm{GRFs}}^{*} = & \arg\min_{\boldsymbol{F}_{\mathrm{r}}} \frac{1}{2}\left\|\boldsymbol{W}_{\mathrm{com}} - \boldsymbol{W}_{\mathrm{com}}^{\mathrm{d}}\right\|_{\boldsymbol{Q}_1}^{2} + \frac{1}{2}\left\|\boldsymbol{F}_{\mathrm{r}}\right\|_{\boldsymbol{Q}_2}^{2} \\ & \text{s.t.} \quad \underline{\boldsymbol{d}} \leq \boldsymbol{C}_{\mathrm{fri}}\boldsymbol{F}_{\mathrm{r}} \leq \bar{\boldsymbol{d}} \end{aligned} \tag{22}$$

where $\boldsymbol{C}_{\mathrm{fri}}$ is a diagonal matrix that encodes the boundaries of the friction cone for the stance legs and the lower and upper bounds of it are represented by $\underline{\boldsymbol{d}}$ and $\bar{\boldsymbol{d}}$ respectively; $\boldsymbol{Q}_1$ and $\boldsymbol{Q}_2$ are the weight matrices for these two objectives respectively. The cost function indicates a trade-off between the two objectives driving the CoM dynamics to reach the target state, and minimizing the GRFs in the optimization problem. The desired CoM wrench $\boldsymbol{W}_{\mathrm{com,d}}^{*}$ after optimazation can be obtained by:

$$\boldsymbol{W}_{\mathrm{com,d}}^{*} = \boldsymbol{J}_{\mathrm{st,com}}^{T}\boldsymbol{F}_{\mathrm{GRFs}}^{*} \tag{23}$$

B. Whole Body planner

When the robot legs have redundant DoF for a specific control task, neglecting leg dynamics can result in the robot losing its ability to perform multiple tasks simultaneously. Additionally, simultaneous handling of multiple tasks is challenging due to potential conflicts between them can result in balance loss. For these reasons, a null space projected whole body planner is introduced for hierarchical full-body acceleration regulation. This method possessed an advantage in efficient computing [13], and its effectiveness is well demonstrated in multiple platforms [18]–[20].

IEEE Robotics and Automation Letters (RA-L) paper, presented at ICRA 2024, Yokohama, Japan. Cite as RA-L paper.

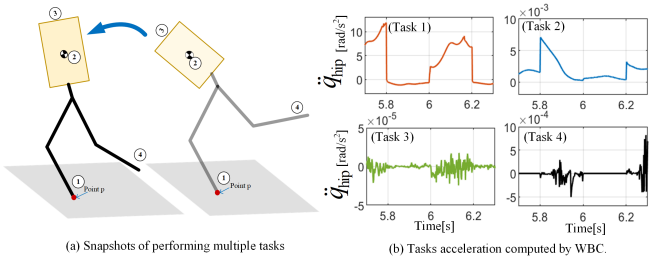

(a) Snapshots of performing multiple tasks (b) Tasks acceleration computed by WBC.

Fig. 3. Multiple task control during dynamic locomotion. (a) presents the snapshots of performing multiple tasks. (b) illustrates the task acceleration $\ddot{\boldsymbol{q}}_{\boldsymbol{i}}$, planned by WBC, for a bipedal robot under external disturbance in a simulator ($\ddot{\boldsymbol{q}}_{\text{hip}}$ represents the angular acceleration of the right leg's hip joint).

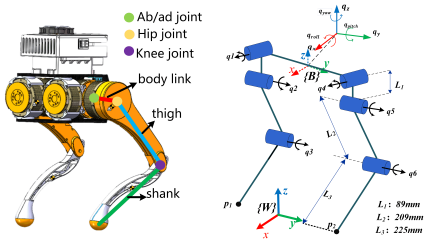

Fig. 4. Point-foot biped robot BRAVER. $\{\boldsymbol{W}\}$ is the world coordinate system and $\{\boldsymbol{B}\}$ is the body attached frame. $\boldsymbol{q}_{\text{i}}$ represents the rotational axis of the i-th DoF.

Consider a floating base system with n DoF and r task coordinates which are defined by

$$\boldsymbol{x}_i = \boldsymbol{f}_i(\boldsymbol{q}) \in \mathbb{R}^{m_i}, \text{ for } i = 1 \dots r \tag{24}$$

The dimension of task i is $m_i \leq n$. The differential mappings from joint velocities to task velocities can be expressed by the Jacobian matrices $\boldsymbol{J}_i(\boldsymbol{q})$ with

$$\dot{\boldsymbol{x}}_i = \boldsymbol{J}_i(\boldsymbol{q})\dot{\boldsymbol{q}}, \quad \boldsymbol{J}_i(\boldsymbol{q}) = \frac{\partial \boldsymbol{f}_i(\boldsymbol{q})}{\partial \boldsymbol{q}} \tag{25}$$

An augmented Jacobian matrix [21] is introduced that stacks, in a top-down manner, all the level-specific Jacobian matrices of the task hierarchy down to the level i.

$$\boldsymbol{J}_i^{\text{aug}}(\boldsymbol{q}) = \begin{pmatrix} \boldsymbol{J}_1(\boldsymbol{q}) \\ \vdots \\ \boldsymbol{J}_i(\boldsymbol{q}) \end{pmatrix} \tag{26}$$

The null-space matrix $\boldsymbol{N}_{\text{prec(i)}}$ [22] containing the null-spaces of all preceding constraints and tasks can be defined as:

$$\boldsymbol{N}_{\text{prec(i)}} = \begin{cases} \boldsymbol{I}, & \text{for } i = 1 \\ \boldsymbol{I} - \boldsymbol{J}_{i-1}^{\text{aug}}(\boldsymbol{q})^T \boldsymbol{J}_{i-1}^{\text{aug}}(\boldsymbol{q})^{M+,T}, & \text{for } i = 2 \dots r \end{cases} \tag{27}$$

where $\boldsymbol{J}_i^{M+} = \boldsymbol{M}^{-1}\boldsymbol{J}_i^{\top}\left(\boldsymbol{J}_i\boldsymbol{M}^{-1}\boldsymbol{J}_i^{\top}\right)^{-1}$ are the individual dynamically-consistent inverses of the prioritized Jacobians [23]. To provide compliant control solutions within the hierarchy, we project the dynamic behavior in task space into the null spaces of the associated joint space through:

$$\ddot{\boldsymbol{q}}_i = \boldsymbol{J}_{i|\text{prec(i)}}^{M+}\left(\ddot{\boldsymbol{x}}_i^d - \dot{\boldsymbol{J}}_i\dot{\boldsymbol{q}} - \boldsymbol{J}_i\ddot{\boldsymbol{q}}_{i-1}^d\right), \quad \boldsymbol{J}_{i|\text{prec(i)}} = \boldsymbol{J}_i\boldsymbol{N}_{\text{prec(i)}} \tag{28}$$

with where $\ddot{\boldsymbol{x}}_i^d$ is the desired acceleration of i-th task. We denote $\ddot{\boldsymbol{q}}^d = \sum_{i=1}^{r}\ddot{\boldsymbol{q}}_i$ as the output of the whole-body acceleration planner. Specifically, in our project, the WBC consists of four tasks. As illustrated in the Fig. 3, the robot places its supporting leg in a fixed position (task 1) and controls the swing leg to follow a predetermined trajectory (task 4) while maintaining the posture (task 2) and global CoM position (task 3) of the body. Furthermore, Fig. 3 also demonstrates the presence of redundant DoF in the bipedal system, i.e., the presence of null spaces in the Jacobian matrix of high-priority tasks relative to low-priority tasks. In order to harmonize the feedforward CoM wrench calculated by centroidal dynamics and the generalized accelerations computed by whole-body planner, a convex optimization function is constructed

$$\begin{aligned} \min_{\boldsymbol{\delta},\boldsymbol{\zeta}} \mathcal{J} \triangleq & \left\|\boldsymbol{W}_{\text{com,d}}^* - \boldsymbol{W}_{\text{com}}\right\|_{\boldsymbol{W}_1}^2 + \left\|\ddot{\boldsymbol{q}}^d - \ddot{\boldsymbol{q}}\right\|_{\boldsymbol{W}_2}^2 + \|\boldsymbol{\zeta}\|_{\boldsymbol{W}_3}^2 \\ \text{s.t.} \quad & \boldsymbol{M}\ddot{\boldsymbol{q}} + \boldsymbol{C}\dot{\boldsymbol{q}} + \boldsymbol{g} = \begin{pmatrix} \boldsymbol{0}_{6\times 1} \\ \boldsymbol{\tau}^{\text{cmd}} \end{pmatrix} + \boldsymbol{J}_{\text{st}}^T\boldsymbol{F}_{\text{r}}, \\ & \boldsymbol{\epsilon} = \boldsymbol{J}_{\text{st}}\ddot{\boldsymbol{q}} + \boldsymbol{J}_{\text{st}}\dot{\boldsymbol{q}}, \\ & -\boldsymbol{\eta} \leq \boldsymbol{J}_{\text{sw}}\ddot{\boldsymbol{q}} + \boldsymbol{J}_{\text{sw}}\dot{\boldsymbol{q}} - \ddot{\boldsymbol{x}}_{\text{sw}} \leq \boldsymbol{\eta}, \\ & \boldsymbol{U}\boldsymbol{F}_{\text{r}} \geq \boldsymbol{0}, \\ & \ddot{\boldsymbol{q}} = \ddot{\boldsymbol{q}}^{\text{d}} + \Delta\ddot{\boldsymbol{q}}, \\ & \boldsymbol{F}_r = \boldsymbol{F}_{\text{GRFs}}^* + \Delta\boldsymbol{F} \end{aligned} \tag{29}$$

where $\boldsymbol{W}_1$, $\boldsymbol{W}_2$ and $\boldsymbol{W}_3$ are diagonal positive definite weight matrices; $\boldsymbol{U}$ is the contact constraint matrix; and $\boldsymbol{\delta} = \begin{bmatrix} \Delta\boldsymbol{F}^T & \Delta\ddot{\boldsymbol{q}}^T \end{bmatrix}^T$ and $\boldsymbol{\zeta} = \begin{bmatrix} \boldsymbol{\epsilon}^T & \boldsymbol{\eta}^T \end{bmatrix}^T$ are the decision variables; In this project, we choose to relax the constraints on contact and swing leg trajectory tracking to avoid infeasibility that may arise when hard constraints conflict with each other [24]. As analyzed in [18], high impedance behaviors in task space have advantages in disturbances rejection. For this reasion, a joint position and velocity feedback control term is added to the final torque command

$$\boldsymbol{\tau}_{\text{min}} \leq \boldsymbol{\tau}^* = \boldsymbol{\tau}^{\text{cmd}} + \boldsymbol{\tau}_{\text{ff}} \leq \boldsymbol{\tau}_{\text{max}} \tag{30}$$

with

$$\boldsymbol{\tau}_{\text{ff}} = \boldsymbol{K}_p^f\left(\boldsymbol{q}^d - \boldsymbol{q}\right) + \boldsymbol{K}_d^f\left(\dot{\boldsymbol{q}}^d - \dot{\boldsymbol{q}}\right) \tag{31}$$

where $\boldsymbol{K}_p^f$ and $\boldsymbol{K}_d^f$ are positive-define diagonal matrices of proportional and derivative gains, respectively; and the desired generalized joint position $\boldsymbol{q}^d$ and joint velocity $\dot{\boldsymbol{q}}^d$ are calculated using KinWBC [18].

IV. Simulations

To evaluate the effectiveness of the algorithm, we conducted several sets of experiments in a simulated environment. The disturbance estimator and control framework presented in this paper is evaluated on our virtual robot, named "BRAVER," as depicted in Fig. 4. The simulation results are obtained using a physical engine provided by Webots R2021b. Both the disturbance estimator and the WBC control loops run in real-time threads at 500 Hz. The robot was configured to perform high-dynamic walking at a stepping frequency of 2.5 Hz and a gait duty cycle of 0.55.

IEEE Robotics and Automation Letters (RA-L) paper, presented at ICRA 2024, Yokohama, Japan. Cite as RA-L paper.

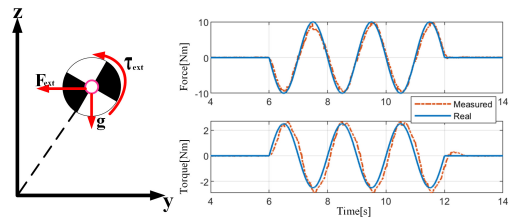

Fig. 5. Estimation of the disturbance through the proposed disturbance estimator.

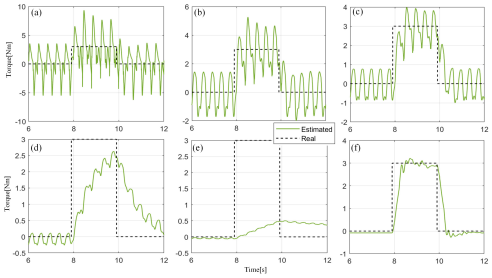

Fig. 6. Comparison between two filtering schemes. (a), (b), (c), (d), and (e) respectively represent the estimation results of a momentum-based observer with cutoff frequencies set to 100 Hz, 10 Hz, 5 Hz, 1 Hz, and 0.1 Hz. (f) represents the estimation results of our scheme, with its cutoff frequency set to 500 Hz and the window width set to $\frac{T}{\Delta t}$.

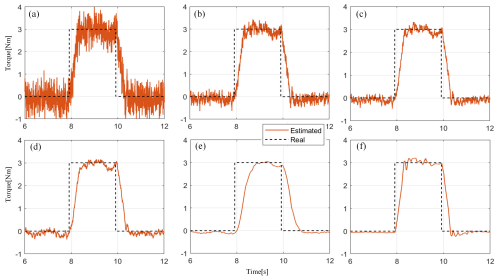

Fig. 7. Comparison between two disturbance observers. The black dashed line represents the actual value of the disturbance, while the red solid line represents the estimated value of the disturbance. (a), (b), (c), (d), and (e) respectively represent the estimation results of a momentum-based observer with cutoff frequencies set to 200 Hz, 100 Hz, 50 Hz, 15 Hz, and 5 Hz. (f) represents the estimation results of the scheme proposed in this paper.

TABLE I
MSE AND VARIANCE RESULTS

Method (Cutoff frequency)	MSE	Var
Momentum observer (200 Hz)	0.6199	0.00160
Momentum observer (100 Hz)	0.5450	0.00120
Momentum observer (50 Hz)	0.5492	0.00140
Momentum observer (15 Hz)	0.6312	0.00110
Momentum observer (5 Hz)	0.8974	0.00029
Our method	0.4876	0.00063

A. External Disturbances Estimation

To investigate the proposed estimator's performance, two case studies have been conducted. The first case study has been carried out by considering a sinusoidal disturbance force along the y-axis, with an amplitude of 10 N and a period $T = 2$ s, on the robot's CoM. In the second case study, a sinusoidal disturbance torque with the same period, and an amplitude of 2.5 Nm is applied along the roll axis at the robot's CoM. The experimental results, depicted in Fig. 5, demonstrate that the estimator is capable of rapidly responding to variations in external disturbances in both cases.

B. Comparison of Filtering Schemes

One major feature of the proposed estimator in this paper is the inclusion of MAF to filter out periodic interaction noise. In order to demonstrate its effectiveness, we conducted comparative experiments between using only a first-order filter and incorporating the MAF. In this experiment, both methods utilized the same approach for estimating foot interaction forces. Due to the significant impact of the cutoff frequency of the momentum observer on its estimation performance, we conducted several sets of experiments with the cutoff frequencies of the momentum observer set at 100 Hz, 10 Hz, 5 Hz, 1 Hz and 0.1 Hz to enhance the persuasiveness of our comparison. The simulation is setup such that robot is walking at a constant speed of 0.05 m/s along x direction and then a disturbance torque is applied on its CoM along the roll direction. Fig. 6 shows the experimental results. As presented in Fig. 6 (a)∼(e), with the decrease in cutoff frequency, the estimator using only a first-order filter shows significant amplitude attenuation but still fails to effectively filter out interaction noise. Our proposed approach demonstrates a notable capability in effectively filtering out interaction noise, as illustrated in Fig. 6 (f).

C. Comparison of Disturbance Observers

Directly utilizing acceleration for CoM's external disturbances estimation is one of the crucial decisions in our proposed observer. The choice is made because acceleration is more sensitive to external disturbances than velocity, and it can avoid introducing integrators that may cause error accumulation. Nevertheless, a reasonable alternative is to use momentum-based observers, which is a widely used technique in robotics. To investigate which estimation scheme provides more accurate behavior, this section presents a simulation case study that compares momentum-based observer with our proposed method. To simulate authentic running environments, in this test, we introduced Gaussian random noise $\mathcal{N}(0,1)$ to the body angular velocity $\boldsymbol{\omega}^{\text{real}}$ and used it as the measured value of angular velocity

$$\boldsymbol{\omega} = \boldsymbol{\omega}^{\text{real}} + \mathcal{N}(0,1) \tag{32}$$

The performance of these two schemes is qualitatively compared by examining which of the two options has a smaller average Mean Squared Error (MSE) as well as the variance of the MSE in multiple rounds of experiments. The formulas for computing MSE and variance (Var) are as follows:

$$MSE = \frac{1}{N}\sum_{\mathrm{i}=1}^{\mathrm{N}}(\hat{y}_i - y_i)^2, Var = \frac{1}{N}\sum_{\mathrm{i}=1}^{\mathrm{N}}(\hat{y}_i - \varrho)^2 \tag{33}$$

where $\hat{y}_i$ and y_i represent the predicted value and real value, respectively; and ϱ represents the sample mean. Similarly,

IEEE Robotics and Automation Letters (RA-L) paper, presented at ICRA 2024, Yokohama, Japan. Cite as RA-L paper.

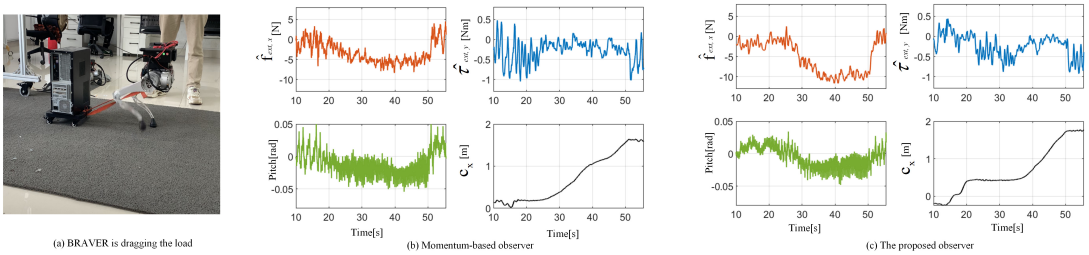

(a) BRAVER is dragging the load (b) Momentum-based observer (c) The proposed observer

Fig. 8. Dragging horizontal load experiment. (a) shows experimental data using the GM-based estimator. (b) presents the experimental data using the proposed estimator. $\hat{\boldsymbol{f}}_{ext,x}$ and $\hat{\boldsymbol{\tau}}_{ext,y}$ represent the external force in the x-direction and the external torque in the pitch direction, respectively. $\boldsymbol{c}_x$ is the CoM position in the x-direction. In this test, both observers used the same cutoff frequency.

we conducted several sets of experiments with the cutoff frequencies of the momentum observer set at 200 Hz, 100 Hz, 50 Hz, 15 Hz and 5 Hz to enhance the persuasiveness of this comparison. Fig. 7 shows the experimental results. The average MSE of 10 run results along with their Var shown in Table. I indicate that the momentum-based observer enhances noise suppression capability by trading off responsiveness, while our proposed estimator can improve upon this issue.

V. Experiments

To evaluate the practicality of the proposed algorithm in a real-world environment, we conducted experimental validation on the point-footed biped robot BRAVER. Prototype experiments were carried out using identical stepping frequency and gait duty factor as those employed in the simulation.

A. Dragging Horizontal Load

In this experiment, a 7 kg load with mobile underpan is attached to the back of the BRAVER with a rope. This test allows to evaluate both disturbance force and torque simultaneously due to the load tension not being fully aligned with the robot's CoM. Fig. 8 summarizes the test results of dragging a constant load. Fig. 8(b) and Fig. 8(c) show experimental data using the momentum-based observer and the proposed observer in this study, respectively. Prior to the complete dragging of the load, minor fluctuations in the robot's state were observed due to the influence of static friction. However, once the robot begun to drag the load, it reached a stable state. The Root Mean Square Error (RSME) for pitch angles in Fig. 8(b) and Fig. 8(c) are $1.3573°$ and $0.8657°$, respectively. Compared to momentum-based observer, the method proposed in this article can reduce fluctuations in disturbance estimation results and Euler angle deviations, thereby enhancing the system's robustness.

B. External Disturbance Perception

To assess the performance of the proposed estimator during high-dynamic motion processes, experiment of external disturbance perception is conducted. In this experiment, a 2kg box was placed on the head of the walking biped robot BRAVER, and it was kept there for approximately 10 s before being removed. The experimental data is shown in Fig. 10. The results indicate that the estimated values of the

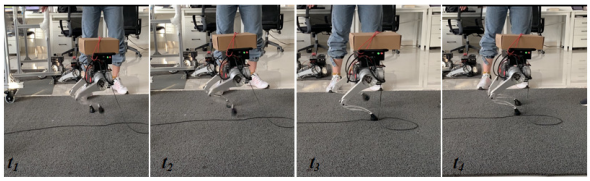

Fig. 9. Snapshots of walking with a 2kg load experiment.

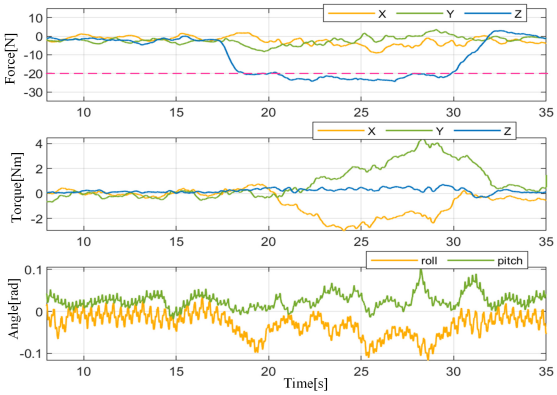

Fig. 10. Results obtained around the pushing action. Force and Torque denote the perturbation force and perturbation torque, respectively, acting at the CoM.

disturbance estimator could converge to the vicinity of the true values when the external disturbances acting on the robot undergo variations. Due to the fact that this external force might not directly act on the CoM of the robot, there was an external torque generated at the CoM of the robot. Fig. (10) demonstrates the consistent relationship between the estimated external torque direction from the estimator and the variations in Euler angles. As shown in Supplementary Video, in the absence of disturbance compensation, the robot proved unable to withstand the external load and eventually experienced a loss of stability. The experiment provides compelling evidence for the effectiveness of our algorithm, even when applied to highly dynamic underactuated platforms.

C. Pushing Recovery

The non-perceived impact test is presented to demonstrate the robustness of our controller. In this experiment, the robot's torso was suddenly hit from the forward direction while walking. After perceiving the shock, the robot quickly adjusted its

IEEE Robotics and Automation Letters (RA-L) paper, presented at ICRA 2024, Yokohama, Japan. Cite as RA-L paper.

Fig. 11. Snapshots of pushing recovery.

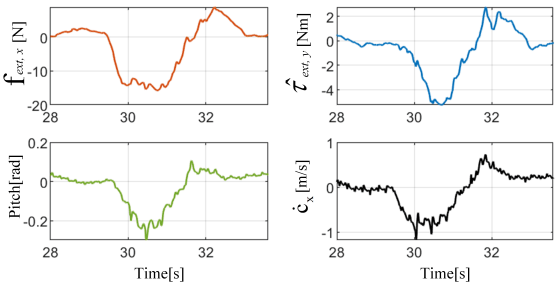

Fig. 12. Results obtained around the pushing action. $\dot{c}_x$ represents the velocity of the robot's CoM in the x-direction.

posture through dynamic feedback and foot point correction. The experimental snapshots are shown in Fig. 11. Fig. 12 indicates that the impact caused the robot's pitch angle to shift over 0.2 rad, and the instantaneous speed of the robot changed over 0.8 m/s. After approximately 1.8 s, BRAVER readjusted to the desired pose, which demonstrated the robustness of the proposed framework.

VI. Conclusion

In this paper, we propose a disturbance perception and resistance framework that enables legged robots to achieve disturbance estimation and compensation during dynamic gait locomotion. The algorithm achieves perception of external disturbances solely based on its own proprioception, without the need for exteroceptive sensors. In contrast to the GM-based disturbance estimators, our estimator directly utilizes acceleration signals for disturbance estimation, which can avoid error accumulation caused by integrators. The proposed disturbance resistance controller incorporates the full-body dynamics, external disturbances and system constraints of the robot. We demonstrated the effectiveness of the proposed estimator and the robustness of the controller through simulation and physical tests on biped robot BRAVER.

References

[1] S.-J. Yi, B.-T. Zhang, D. Hong, and D. D. Lee, "Online learning of a full body push recovery controller for omnidirectional walking," in *2011 11th IEEE-RAS International Conference on Humanoid Robots*, 2011, pp. 1–6.

[2] V. Prahlad, G. Dip, and C. Meng-Hwee, "Disturbance rejection by online zmp compensation," *Robotica*, vol. 26, no. 1, pp. 9–17, 2008.

[3] S.-H. Hyon and G. Cheng, "Disturbance rejection for biped humanoids," pp. 2668–2675, 2007.

[4] Y. Wang, R. Xiong, Q. Zhu, and J. Chu, "Compliance control for standing maintenance of humanoid robots under unknown external disturbances," in *2014 IEEE International Conference on Robotics and Automation (ICRA)*, 2014, pp. 2297–2304.

[5] J. Pratt, J. Carff, S. Drakunov, and A. Goswami, "Capture point: A step toward humanoid push recovery," in *2006 6th IEEE-RAS International Conference on Humanoid Robots*, 2006, pp. 200–207.

[6] S. Dafarra, F. Romano, and F. Nori, "Torque-controlled stepping-strategy push recovery: Design and implementation on the icub humanoid robot," in *2016 IEEE-RAS 16th International Conference on Humanoid Robots (Humanoids)*. IEEE, 2016, pp. 152–157.

[7] A. De Luca, A. Albu-Schaffer, S. Haddadin, and G. Hirzinger, "Collision detection and safe reaction with the dlr-iii lightweight manipulator arm," in *2006 IEEE/RSJ International Conference on Intelligent Robots and Systems*, 2006, pp. 1623–1630.

[8] A. De Luca and F. Flacco, "Integrated control for phri: Collision avoidance, detection, reaction and collaboration," in *2012 4th IEEE RAS & EMBS International Conference on Biomedical Robotics and Biomechatronics (BioRob)*, 2012, pp. 288–295.

[9] J. Englsberger, "Combining reduced dynamics models and whole-body control for agile humanoid locomotion," Ph.D. dissertation, 12 2016.

[10] J. Englsberger, G. Mesesan, and C. Ott, "Smooth trajectory generation and push-recovery based on divergent component of motion," in *2017 IEEE/RSJ International Conference on Intelligent Robots and Systems (IROS)*, 2017, pp. 4560–4567.

[11] M. Focchi, R. G. Orsolino, M. Camurri, V. Barasuol, C. Mastalli, D. Caldwell, and C. Semini, "Heuristic Planning for Rough Terrain Locomotion in Presence of External Disturbances and Variable Perception Quality," in *Springer Track in Advanced Robotics series*, 2018. [Online]. Available: https://hal.science/hal-02086090

[12] V. Morlando, A. Teimoorzadeh, and F. Ruggiero, "Whole-body control with disturbance rejection through a momentum-based observer for quadruped robots," *Mechanism and Machine Theory*, vol. 164, p. 104412, 2021.

[13] D. Kim, J. Lee, J. Ahn, O. Campbell, H. Hwang, and L. Sentis, "Computationally-robust and efficient prioritized whole-body controller with contact constraints," in *2018 IEEE/RSJ International Conference on Intelligent Robots and Systems (IROS)*, 2018, pp. 1–8.

[14] Z. Zhu, W. Zhu, G. Zhang, T. Chen, Y. Li, X. Rong, R. Song, D. Qin, Q. Hua, and S. Ma, "Design and control of braver: a bipedal robot actuated via proprioceptive electric motors," *Autonomous Robots*, pp. 1–15, 2023.

[15] A. De Luca, A. Albu-Schaffer, S. Haddadin, and G. Hirzinger, "Collision detection and safe reaction with the dlr-iii lightweight manipulator arm," in *2006 IEEE/RSJ International Conference on Intelligent Robots and Systems*, 2006, pp. 1623–1630.

[16] G. Bledt, P. M. Wensing, S. Ingersoll, and S. Kim, "Contact model fusion for event-based locomotion in unstructured terrains," in *2018 IEEE International Conference on Robotics and Automation (ICRA)*, 2018, pp. 4399–4406.

[17] Z. Yu, Q. Zhou, X. Chen, Q. Li, L. Meng, W. Zhang, and Q. Huang, "Disturbance rejection for biped walking using zero-moment point variation based on body acceleration," *IEEE Transactions on Industrial Informatics*, vol. 15, no. 4, pp. 2265–2276, 2019.

[18] D. Kim, S. J. Jorgensen, J. Lee, J. Ahn, J. Luo, and L. Sentis, "Dynamic locomotion for passive-ankle biped robots and humanoids using whole-body locomotion control," *The International Journal of Robotics Research*, vol. 39, no. 8, pp. 936–956, 2020.

[19] T. Chen, Y. Li, X. Rong, G. Zhang, H. Chai, J. Bi, and Q. Wang, "Design and control of a novel leg-arm multiplexing mobile operational hexapod robot," *IEEE Robotics and Automation Letters*, vol. 7, no. 1, pp. 382–389, 2021.

[20] Q. Li, L. Qian, S. Wang, P. Sun, and X. Luo, "Towards generation and transition of diverse gaits for quadrupedal robots based on trajectory optimization and whole-body impedance control," *IEEE Robotics and Automation Letters*, vol. 8, no. 4, pp. 2389–2396, 2023.

[21] B. Siciliano and J.-J. Slotine, "A general framework for managing multiple tasks in highly redundant robotic systems," in *Fifth International Conference on Advanced Robotics 'Robots in Unstructured Environments*, 1991, pp. 1211–1216 vol.2.

[22] B. Henze, A. Dietrich, and C. Ott, "An approach to combine balancing with hierarchical whole-body control for legged humanoid robots," *IEEE Robotics and Automation Letters*, vol. 1, no. 2, pp. 700–707, 2016.

[23] L. Sentis and O. Khatib, "Synthesis of whole-body behaviors through hierarchical control of behavioral primitives," *International Journal of Humanoid Robotics*, vol. 2, no. 04, pp. 505–518, 2005.

[24] S. Fahmi, C. Mastalli, M. Focchi, and C. Semini, "Passive whole-body control for quadruped robots: Experimental validation over challenging terrain," *IEEE Robotics and Automation Letters*, vol. 4, no. 3, pp. 2553–2560, 2019.

IEEE Robotics and Automation Letters (RA-L) paper, presented at ICRA 2024, Yokohama, Japan. Cite as RA-L paper.